Step-by-Step Controller Design for *LCL*-Type Grid-Connected Inverter with Capacitor–Current-Feedback Active-Damping

Chenlei Bao, Xinbo Ruan, *Senior Member, IEEE*, Xuehua Wang, *Member, IEEE*, Weiwei Li, *Student Member, IEEE*, Donghua Pan, *Student Member, IEEE*, and Kailei Weng

***Abstract*—The injected grid current regulator and active damping of the *LCL* filter are essential to the control of *LCL*-type grid-connected inverters. Generally speaking, the current regulator guarantees the quality of the injected grid current, and the active damping suppresses the resonance peak caused by the *LCL* filter and makes it easier to stabilize the whole system. Based on the proportional-integral (PI) and proportional-resonant (PR) compensator together with capacitor–current-feedback active-damping which are widely used for their effectiveness and simple implementations, this paper proposes a simple step-by-step controller design method for the *LCL*-type grid-connected inverter. By carefully dealing with the interaction between the current regulator and active damping, the complete satisfactory regions of the controller parameters for meeting the system specifications are obtained, and from which the controller parameters can be easily picked out. Based on these satisfactory regions, it is more convenient and explicit to optimize the system performance. Besides, the insight of tuning the controller parameters from these satisfactory regions is also discussed. Simulation and experimental results verify the proposed step-by-step design method.**

***Index Terms*—Active damping, controller design, grid-connected inverter, *LCL* filter, single-phase.**

I. Introduction

NOWADAYS, distributed power generation system (DPGS) based on renewable energy, such as wind energy and solar energy, has been drawing more and more attentions, for its environmental friendly features. As the interface between the DPGS and power grid, grid-connected inverter plays an important role in injecting high-quality power into the grid [1]. An L filter or *LCL* filter is usually placed between the inverter and the grid to attenuate the switching frequency harmonics produced by the grid-connected inverter. Compared with L filter, *LCL* filter has better attenuation of the switching frequency harmonics, which usually yields lower volume and costs [2], [3]. However, the inherent resonance of the *LCL* filter requires proper damping methods to avoid the possible instability of the system [4], [5].

A direct way to damp the resonance of the *LCL* filter is introducing a passive resistor to be in series or parallel with the filter inductors or filter capacitor, which is called passive-damping method. Among which, adding a resistor in series with the filter capacitor has been widely adopted for its simplicity and relatively low power loss. However, it will weaken the switching harmonic attenuation ability [5]–[8]. Adding a resistor in parallel with the filter capacitor will not impair the low-and high-frequency characteristics of the *LCL* filter, but the power loss brought by this resistor is too large to be accepted [9].

In order to avoid the power loss resulted from the passive resistor, the concept of virtual resistor was proposed in place of the passive resistor, and the virtual resistor can be realized through proper control schemes [10]. Such methods are called active-damping methods [11], [12]. It was proved that the proportional feedback of the filter capacitor current is equivalent to a resistor in parallel with the filter capacitor [10]. Besides, multiple-state feedback can also be used to achieve *LCL* resonance damping, fast dynamic response, and reasonable robustness [13]. Multiple-state feedback can be formalized within general theoretical frameworks of state-space control by properly specified pole placements [13]–[15], predictive control by proper deadbeat control laws and observers [16]–[18], or h-infinity control by solving one single optimization problem with specified control constraints [19]–[23], etc. In this paper, the capacitor–current-feedback active-damping is studied due to its effectiveness, simple implementation, and wide application [24]–[26]. The capacitor–current feedback coefficient should be selected with great caution, since a too small one cannot damp the resonance effectively, and a too large one may result in system instability [26].

Besides the system stability, high-quality injected power is another essential object in the control of the grid-connected inverter. Therefore, the design of the injected grid current regulator is very important. The primary goals of the injected grid current regulator are to minimize the steady-state error, achieve the best possible dynamic performance, minimize the harmonics in the

Manuscript received September 13, 2012; revised November 21, 2012, January 22, 2013, and March 24, 2013; accepted April 24, 2013. Date of current version September 18, 2013. This work was supported by the National Natural Science Foundation of China under Award 50837003 and Award 51007027, and the National Basic Research Program of China under Award 2009CB219706. Recommended for publication by Associate Editor S. Williamson.

C. Bao, X. Wang, W. Li, D. Pan, and K. Weng are with the State Key Laboratory of Advanced Electromagnetic Engineering and Technology, Huazhong University of Science and Technology, Wuhan 430074, China (e-mail: baochenlei@hust.edu.cn; wang.xh@hust.edu.cn; Weiwei_Li@hust.edu.cn; pan_dh@hust.edu.cn; lswkl9331@hust.edu.cn).

X. Ruan is with the State Key Laboratory of Advanced Electromagnetic Engineering and Technology, Huazhong University of Science and Technology, Wuhan 430074, China, and also with the Aero-Power Sci-Tech Center, College of Automation Engineering, Nanjing University of Aeronautics and Astronautics, Nanjing 210016, China (e-mail: ruanxb@ hust.edu.cn).

Color versions of one or more of the figures in this paper are available online at http://ieeexplore.ieee.org.

Digital Object Identifier 10.1109/TPEL.2013.2262378

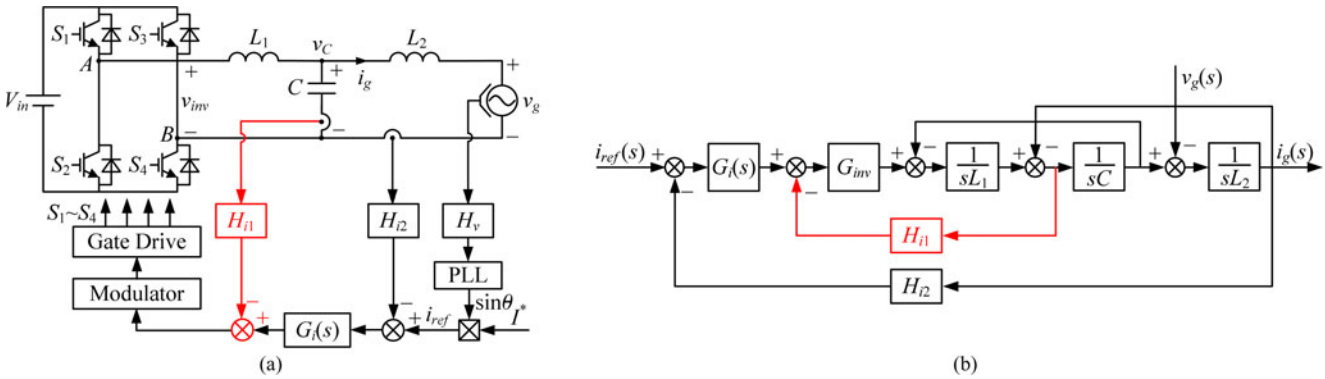

Fig. 1. *LCL*-type single-phase grid-connected inverter based on capacitor–current-feedback active-damping. (a) Schematic diagram. (b) ASM.

injected grid current, and so on [27]. Generally, these system performance and stability margin can be specified by steady-state error, crossover frequency (f_c), phase margin (PM), and gain margin (GM) of the system. As a consequence, these terms will be frequently referred during the design of the current regulator and capacitor–current-feedback active-damping in this paper.

In recent years, the design of current regulator and capacitor–current-feedback active-damping for *LCL*-type grid-connected inverter has been extensively discussed. The root-locus design method was used in [24], but the controller parameters were partially tuned according to the simulations and experiments. Both proportional-integral (PI) and proportional-resonant (PR) current regulators were investigated in [28], and pole-zero cancellation along with pole placement method was introduced. The design procedure was complex, and the feedbacks of the capacitor current and injected grid current (only two state variables) could not provide complete information of the three-order *LCL* filter to assign all the poles in the optimal positions. Therefore, parameter adjustments were necessary to obtain an optimized result. Symmetrical optimum (SO) was used to design the current regulator whereas the *LCL* filter was approximated to the L filter, and then the capacitor–current feedback coefficient could be determined easily using root-locus method [26], [29]. SO mainly focused on the PM, and did not pay enough attention to the specifications of steady-state error, f_c, and GM. The active-damping method of capacitor–current feedback would deteriorate the PM to obtain sufficient GM, thus the controller parameters designed by SO may not be good enough, some further work was needed to obtain an optimized result. Besides, technical optimum was also widely used in designing controller parameters especially for second-order systems, but it was not convenient for designing the controller parameters of high-order systems such as *LCL*-type grid-connected inverters, and may lead to a poor disturbance rejection system [11]. In fact, the frequency responses of the current regulator and capacitor–current-feedback active-damping interact with each other on the PM and GM of the system, thus the design and optimization of the current regulator and capacitor–current feedback coefficient are coupled.

This paper analyzes the characteristics of the controller parameters of PI and PR regulators for the injected grid current closed-loop together with capacitor–current-feedback active-damping [26]–[31] in detail and proposes a simple step-by-step design and optimized method of the current regulator and capacitor–current feedback coefficient for the *LCL*-type grid-connected inverter. Performance improvements over state-space control, predictive control, h-infinity, etc., are beyond the scope of this paper and might be discussed in future work. By carefully dealing with the interaction between the current regulator and active-damping, the satisfactory regions of the controller parameters can be obtained with the given specifications of the system performance and stability margin, which reveal the boundaries of the controller parameters and make the choices and optimizations of these parameters more convenient and explicit. This paper is organized as follows. In Section II, the mathematical model of the *LCL*-type grid-connected inverter using averaged switch model (ASM) is derived. Based on the derived ASM, the relationship between the controller parameters and the system loop gain is analyzed preliminarily in Section III. In Section IV, a step-by-step design method of the PI injected grid current regulator and capacitor–current-feedback active-damping is presented in detail. In Section V, the proposed method is extended to design the controllers based on PI current regulator plus grid voltage feedforward scheme, and PR current regulator, respectively. In Section VI, design examples and simulation results of an *LCL*-type single-phase grid-connected inverter are presented. The experimental results are presented in Section VII and the conclusion is given in Section VIII.

II. Modeling the *LCL*–Type Single-Phase Grid-Connected Inverter

Fig. 1(a) shows the topology and the control scheme of an *LCL*-type single-phase grid-connected inverter. A typical single-phase voltage-source inverter (VSI) is connected to the grid through an *LCL* filter, which is composed of the inverter-side inductor L_1, filter capacitor C, and grid-side inductor L_2. The equivalent series resistors of L_1, C, and L_2 are relatively small and ignored here. A phase-locked loop (PLL) is used to synchronize the reference of the injected grid current $i_{\rm ref}$ with the grid voltage v_g. H_v and H_{i2} are the gains of the grid voltage and injected grid current sensors, respectively. $G_i(s)$ is the injected grid current regulator. The feedback of the filter capacitor current

is adopted to damp the resonance peak caused by the *LCL* filter, and H_{i1} is the feedback coefficient. Unipolar sinusoidal pulsewidth modulation (SPWM) is used for the grid-connected inverter. An outer-loop power control is usually introduced to automatically adjust the current reference amplitude I^*. This is beyond the scope of this paper and will not be discussed, and the current reference amplitude I^* is directly given here.

The resonance frequency of the *LCL* filter f_r is derived as

$$f_r = \frac{1}{2\pi}\sqrt{\frac{L_1+L_2}{L_1L_2C}}. \tag{1}$$

Fig. 1(b) shows the ASM of the *LCL*-type grid-connected inverter, where $G_{\rm inv}$ is the transfer function of the inverter bridge. The switching frequency of VSI is assumed to be sufficiently high, thus $G_{\rm inv}$ can be approximated as $V_{\rm in}/V_{\rm tri}$, where $V_{\rm in}$ is the dc-link voltage and $V_{\rm tri}$ is the amplitude of the triangle carrier wave. According to Mason's gain formula [32], the injected grid current i_g can be derived as

$$\begin{aligned} i_g(s) &= \frac{1}{H_{i2}}\frac{T(s)}{1+T(s)}i_{\rm ref}(s) - \frac{G_g(s)}{1+T(s)}v_g(s) \\ &\triangleq i_{g1}(s) + i_{g2}(s) \end{aligned} \tag{2}$$

where $T(s)$ is the loop gain of the system and is expressed as

$$T(s) = \frac{H_{i2}G_{\rm inv}G_i(s)}{s^3L_1L_2C + s^2L_2CH_{i1}G_{\rm inv} + s(L_1+L_2)} \tag{3}$$

and $G_g(s)$ is expressed as

$$G_g(s) = \frac{s^2L_1C + sCG_{\rm inv}H_{i1} + 1}{s^3L_1L_2C + s^2L_2CH_{i1}G_{\rm inv} + s(L_1+L_2)}. \tag{4}$$

i_{g1} is related to the injected grid current reference $i_{\rm ref}$ and i_{g2} is related to the grid voltage v_g. i_{g1} and i_{g2} are expressed as

$$i_{g1}(s) = \frac{1}{H_{i2}}\frac{T(s)}{1+T(s)}i_{\rm ref}(s) \tag{5}$$

$$i_{g2}(s) = -\frac{G_g(s)}{1+T(s)}v_g(s). \tag{6}$$

III. Frequency Responses of the Current Regulator and Capacitor–Current-Feedback Active-Damping

According to (3), the bode diagram of the uncompensated loop gain is depicted in Fig. 2. As seen, introducing the feedback of the filter capacitor current can effectively damp the resonance peak, and it only affects the magnitude of the loop gain at the neighbor of the resonance frequency. However, this active-damping method has significant impact on the phase of the loop gain and the phase decreases at the frequencies lower than the resonance frequency. A larger capacitor–current feedback coefficient leads to better damping of the resonance peak, but results in a larger negative phase shift.

The crossover frequency f_c is typically restricted lower than f_s considering the effect of attenuating high-frequency noise, where f_s is the switching frequency of the inverter [9], and the resonance frequency of the *LCL* filter f_r is usually constrained between 1/4 and 1/2 of the equivalent switching frequency of the inverter (when unipolar SPWM is adopted, the equivalent switching frequency is $2f_s$), for the sake of effective harmonics suppression and good dynamic response. Therefore, for a properly designed *LCL*-type grid-connected inverter, the crossover frequency f_c will be lower than the resonance frequency f_r, thus the influence of the filter capacitor can be ignored when calculating the magnitude of the loop gain at f_c and the frequencies lower than f_c, i.e., the magnitude of $T(s)$ can be approximated as

$$|T(s)| \approx \left|\frac{H_{i2}G_{\rm inv}G_i(s)}{s(L_1+L_2)}\right|. \tag{7}$$

PI compensator is adopted as the injected grid current regulator and the transfer function of $G_i(s)$ is given by

$$G_i(s) = K_p + \frac{K_i}{s}. \tag{8}$$

According to (8), the bode diagram of PI compensator is depicted in Fig. 3. As seen, at the frequencies around the corner frequency f_L which is expressed as $f_L = K_i/(2\pi K_p)$, the slope

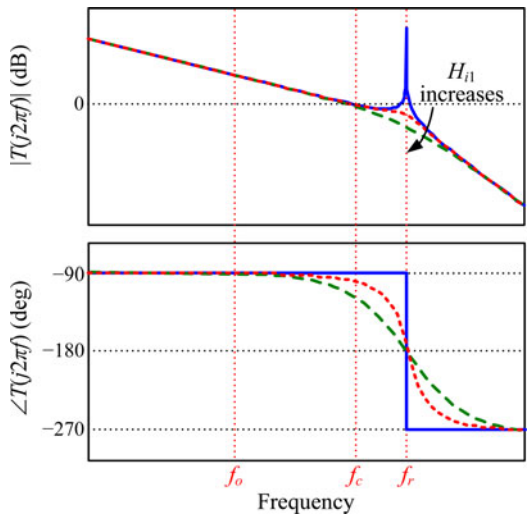

Fig. 2. Bode diagram of the loop gain without compensation.

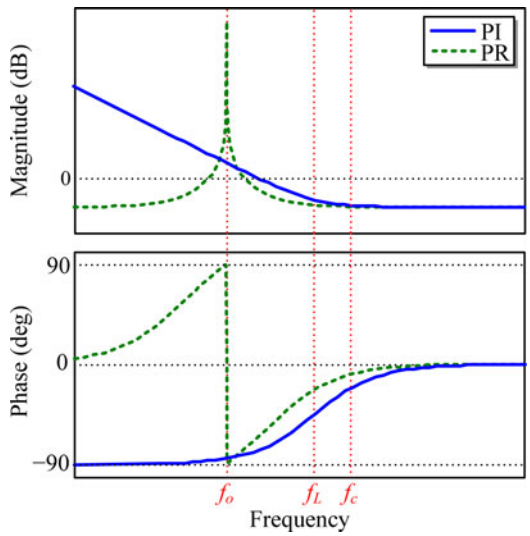

Fig. 3. Bode diagram of PI and PR compensators.

of the magnitude changes from −20 to 0 dB/dec, and the phase escalates from − 90° up to 0°. To avoid the decrease of the PM resulted from PI compensator, f_L is suggested to be set sufficiently lower than f_c. Thus, the magnitude of $G_i(s)$ can be approximated to K_p at f_c and the frequencies higher than f_c. Because the magnitude of the loop gain $T(s)$ is unity at f_c, substituting $|G_i(s)| \approx K_p$ into (7) yields

$$K_p \approx \frac{2\pi f_c (L_1 + L_2)}{H_{i2} G_{\text{inv}}}. \tag{9}$$

Equation (9) shows that f_c is approximatively proportional to K_p. Therefore, a larger K_p means a faster dynamic response and a larger loop gain at low frequencies.

IV. Step-by-Step Design Method of the PI Current Regulator and Capacitor–Current Feedback Coefficient

A step-by-step interactive and optimized design method of the PI injected grid current regulator and capacitor–current feedback coefficient is proposed in this section with careful examinations of the steady-state error and stability margin of the system.

A. Requirement of Steady-State Errors

The steady-state error of i_g at the fundamental frequency f_o is an important index of the controller parameters design. As given by (2), the injected grid current i_g consists of i_{g1} and i_{g2}. For the convenience of illustration, the fundamental components of i_g, i_{g1}, i_{g2}, and v_g are denoted by $i_{g(1)}, i_{g1(1)}, i_{g2(1)}$, and $v_{g(1)}$, respectively. If T_{fo}, the magnitude of the loop gain at f_o is sufficiently large, for instance $T_{fo} \geq 40$ dB, then $1 + T(j2\pi f_o) \approx T(j2\pi f_o)$. Thus, according to (5), $i_{g1(1)} \approx i_{\text{ref}} / H_{i2}$. As the influence of the filter capacitor is negligible at f_o, considering (3), (4), and (6), $i_{g2(1)}$ can be approximated as

$$i_{g2(1)} \approx -\frac{v_{g(1)}}{H_{i2} G_{\text{inv}} G_i (j2\pi f_o)}. \tag{10}$$

When PI compensator is adopted, $G_i(j2\pi f_o) \approx K_i/(j2\pi f_o)$, so $i_{g2(1)} \approx -j2\pi f_o\, v_{g(1)}/(H_{i2} G_{\text{inv}} K_i)$, which means that $i_{g2(1)}$ is 90° lagging to $v_{g(1)}$. Fig. 4(a) shows the phasor diagrams of $i_{g(1)}, i_{g1(1)}, i_{g2(1)}, v_{g(1)}$, and i_{ref}, where $i_{g1(1)}$ and i_{ref} are in the same direction as explained earlier, and i_{ref} leads $v_{g(1)}$ by the phase angle θ. θ is usually set according to the power flow requirement of the system. As seen, it is $i_{g2(1)}$ that makes $i_{g(1)}$ away from $i_{g1(1)}$. The steady-state errors can be defined as the amplitude error E_A and the phase error δ. Referring to Fig. 4(a), the amplitude error E_A can be expressed as

$$E_A = \left| \frac{H_{i2} I_g - I_{\text{ref}}}{I_{\text{ref}}} \right| = \left| \frac{H_{i2}}{I_{\text{ref}}} \sqrt{I_{g1}^2 + I_{g2}^2 - 2 I_{g1} I_{g2} \sin\theta} - 1 \right| \tag{11}$$

where $I_{\text{ref}}, I_g, I_{g1}, I_{g2}$, are the rms values of $i_{\text{ref}}, i_{g(1)}, i_{g1(1)}$, and $i_{g2(1)}$, respectively. As $i_{g1(1)} \approx i_{\text{ref}} / H_{i2}$, solving (11), the upper boundary of I_{g2} constrained by $E_A, I_{g2\max\_\text{EAPI}}$ is

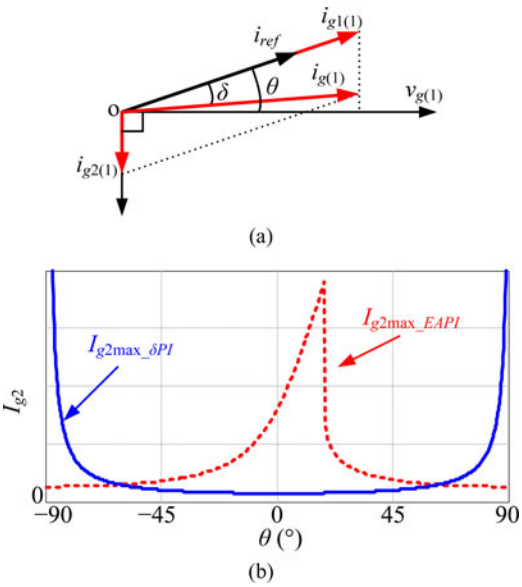

Fig. 4. Steady-state error with PI compensator. (a) Phasor diagrams of $i_{g(1)}, i_{g1(1)}, i_{g2(1)}, v_{g(1)}$, and i_{ref}. (b) Variations of $I_{g2\max\_\text{EAPI}}$ and $I_{g2\max\_\delta\text{PI}}$ for given E_A and δ when θ varies.

derived in the Appendix, and is expressed as

$$I_{g2\,\max\_\text{EAPI}} \approx \begin{cases} \dfrac{I_{\text{ref}}}{H_{i2}} \left(\sin\theta + \sqrt{(E_A+1)^2 - \cos^2\theta} \right) \\ \quad -90^\circ \leq \theta < \theta_1 \\ \dfrac{I_{\text{ref}}}{H_{i2}} \left(\sin\theta - \sqrt{(E_A-1)^2 - \cos^2\theta} \right) \\ \quad \theta_1 \leq \theta \leq 90^\circ \end{cases} \tag{12}$$

where $\theta_1 = \arcsin\sqrt{2E_A - E_A^2}$ and as no active power is absorbed from the grid, $\theta \in [-90^\circ, 90^\circ]$.

According to Fig. 4(a) and sine law, sinδ is given as

$$\sin\delta = \frac{I_{g2}}{I_{g1}} \left| \sin(90^\circ + \theta - \delta) \right|. \tag{13}$$

From Fig. 4(a) and (13), it is obvious that $\delta = 0$ when $\theta = \pm 90^\circ$ and when $\theta \neq \pm 90^\circ$, the upper boundary of I_{g2} constrained by δ, $I_{g2\max\_\delta\text{PI}}$, can be expressed as

$$I_{g2\,\max\_\delta\text{PI}} \approx \frac{I_{\text{ref}}}{H_{i2}} \left| \frac{\sin\delta}{\cos(\theta - \delta)} \right|. \tag{14}$$

According to (12) and (14), the variations of $I_{g2\max\_\text{EAPI}}$ and $I_{g2\max\_\delta\text{PI}}$ when θ varies are depicted as Fig. 4(b). As E_A and δ should be small for a properly designed inverter, it is obvious that $I_{g2\max\_\text{EAPI}}$ is minimum when $\theta \approx \pm 90^\circ$ and $I_{g2\max\_\delta\text{PI}}$ is minimum when $\theta \approx 0^\circ$. The specific requirement of the steady-state error can be easily simplified to the worst situation of I_{g2}, $\min\{I_{g2\max\_\text{EAPI}}, I_{g2\max\_\delta\text{PI}}\}$, in the range of θ which is concerned.

Considering (7) and (10), I_{g2} can be approximated as

$$I_{g2} \approx \frac{V_g}{H_{i2} G_{\text{inv}} |G_i(j2\pi f_o)|} \approx \frac{V_g}{2\pi f_o (L_1 + L_2) |T(j2\pi f_o)|} \tag{15}$$

where V_g is the rms value of $v_{g(1)}$.

Equation (15) can be rewritten as

$$T_{fo} = 20\log_{10}\left|T\left(j2\pi f_o\right)\right| \approx 20\log_{10}\frac{V_g}{2\pi f_o\left(L_1+L_2\right)I_{g2}} \tag{16}$$

where the unit of T_{fo} is dB. From (16), it is found that I_{g2} is related to T_{fo}, thus the requirement of the steady-state error can be further specified by the requirement of T_{fo} after $\min\{I_{g2\max\_\mathrm{EAPI}}, I_{g2\max\_\delta\mathrm{PI}}\}$ is confirmed.

B. Controller Parameters Constrained by Steady-State Error and Stability Margin

According to (7) and (8), T_{fo} is expressed as

$$T_{fo} = 20\log_{10}\left|T\left(j2\pi f_o\right)\right| = 20\log_{10}\left|\frac{H_{i2}G_{\mathrm{inv}}\left(K_p+\frac{K_i}{j2\pi f_o}\right)}{j2\pi f_o\left(L_1+L_2\right)}\right|. \tag{17}$$

Substituting (9) into (17) leads to

$$K_i = \frac{4\pi^2 f_o\left(L_1+L_2\right)}{H_{i2}G_{\mathrm{inv}}}\sqrt{\left(10^{\frac{T_{fo}}{20}}f_o\right)^2 - f_c^2}. \tag{18}$$

According to (3), the PM of the system can be expressed as

$$\mathrm{PM} = 180^\circ + \angle\frac{H_{i2}G_{\mathrm{inv}}G_i\left(s\right)}{s^3L_1L_2C + s^2L_2CH_{i1}G_{\mathrm{inv}} + s\left(L_1+L_2\right)}\bigg|_{s=j2\pi f_c}. \tag{19}$$

Substituting (8) into (19), leads to

$$\mathrm{PM} = \arctan\frac{2\pi L_1\left(f_r^2-f_c^2\right)}{H_{i1}G_{\mathrm{inv}}f_c} - \arctan\frac{K_i}{2\pi f_c K_p}. \tag{20}$$

Equation (20) can be rewritten as

$$K_i = 2\pi f_c K_p\frac{2\pi L_1\left(f_r^2-f_c^2\right) - G_{\mathrm{inv}}f_cH_{i1}\tan\mathrm{PM}}{2\pi L_1\left(f_r^2-f_c^2\right)\tan\mathrm{PM} + G_{\mathrm{inv}}f_cH_{i1}}. \tag{21}$$

Substituting (9) and (18) into (21), leads to

$$H_{i1} = \frac{2\pi L_1\left(f_r^2-f_c^2\right)\left(f_c^2 - f_o\sqrt{\left(10^{\frac{T_{fo}}{20}}f_o\right)^2 - f_c^2}\tan\mathrm{PM}\right)}{G_{\mathrm{inv}}f_c\left(f_c^2\tan\mathrm{PM} + f_o\sqrt{\left(10^{\frac{T_{fo}}{20}}f_o\right)^2 - f_c^2}\right)}. \tag{22}$$

As seen from Fig. 2, the phase of the uncompensated loop gain $T(s)$ runs across -180° at f_r, thus the GM of the system can be obtained as

$$\mathrm{GM} = -20\log_{10}\left|T\left(j2\pi f_r\right)\right| \tag{23}$$

where the unit of GM is dB.

It should be noticed that the magnitude of the loop gain $T(s)$ shown in (7) is not accurate at f_r. Therefore, substituting (3), the expression of the loop gain without approximation and (9) into (23), yields

$$H_{i1} = 10^{\frac{\mathrm{GM}}{20}}\cdot\frac{2\pi f_c L_1}{G_{\mathrm{inv}}}. \tag{24}$$

C. PWM Constraint

In PWM systems, the maximum rate of the change of the reference should not equal or exceed that of the carrier signal [31], [34]–[39]. For an analog system, this requirement must be met for a fixed PWM switching frequency. In this case, the current ripple of i_g is small and the maximum rate of the modulation wave mainly affects H_{i1}. Therefore, the critical gain of H_{i1} is

$$H_{i1(\max)} = \frac{4V_{\mathrm{tri}}f_sL_1}{V_{\mathrm{in}}}. \tag{25}$$

D. Design of the PI Compensator and Capacitor–Current Feedback Coefficient

Thus, a step-by-step controller design procedure based on the examinations of the steady-state error and stability margin of the system is proposed as follows:

Step 1) Determine the specifications of the loop gain, specifically, T_{fo} by the requirement of the steady-state error, PM by the requirements of the dynamic response and robustness of the system, and GM by the requirement of the robustness.

As shown in Fig. 4, the steady-state errors are more remarkable in light power cases, thus T_{fo} can be confirmed by the specific situation in the standards, for instance, power factor (PF) in 10% of the rated power case must be larger than 0.85 [41] or PF in half power case must be larger than 0.98 [42], and T_{fo} can also be confirmed by requirements of customers. In general, PM in the range of (30°, 60°) is adopted for good dynamic response and robustness, GM $\geq 3-6$ dB is introduced to ensure the system robust stability.

Step 2) Based on the above given specifications, draw the satisfactory region of f_c and H_{i1} according to (22), (24), and (25).

According to the *LCL* filter design methods proposed in [6] and [40], the specified requirements of the *LCL* filter are presented as follows: 1) L_1+L_2 is less than 0.1 pu to limit the ac voltage drop, 2) the reactive power is less than 5% of the rated power, 3) the converter-side current ripple is less than 30% of the rms value of the injected grid current at rated power, 4) the resonance frequency is in the range of 1/4 and 1/2 of the equivalent switching frequency; 5) and the switching harmonics are less than 0.3% of the fundamental current at rated power [41]. Table I shows the parameters of an *LCL*-type single-phase grid-connected inverter.

With the above inverter parameters, the satisfactory region of f_c and H_{i1} is depicted in Fig. 5. The area upon the dashed line meets the requirement of the GM and the area under the solid line meets the

TABLE I
SYSTEM PARAMETERS

Parameter	Symbol	Value	Parameter	Symbol	Value
Grid voltage (RMS)	V_g	220 V	Dc-link voltage	V_{in}	360 V
Fundamental frequency	f_o	50 Hz	Amplitude of triangle carrier wave	V_{tri}	3 V
Inverter-side inductor	L_1	600 μH	Switching frequency	f_s	10 kHz
Filter capacitor	C	10 μF	Equivalent switching frequency	-	20 kHz (unipolar)
Grid-side inductor	L_2	150 μH	Output power	P_o	6 kW
Resonance frequency	f_r	4.6 kHz	Injected grid current feedback coefficient	H_{i2}	0.15

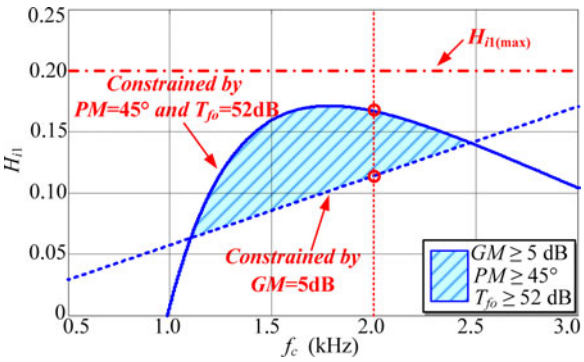

Fig. 5. Region of f_c and H_{i1} constrained by GM, PM, and T_{fo} when PI compensator is adopted.

requirements of the PM and T_{fo}. Thus, the shaded area between these two lines includes all the possible H_{i1} and f_c satisfying the aforementioned specifications of the loop gain. From Fig. 5, it can be seen that:

1) when f_c increases, the lower boundary of the shaded area increases, as a larger H_{i1} is needed for a larger f_c to obtain the same GM;
2) when f_c increases, the upper boundary of the shaded area ascends first and then descends. With the increase of f_c, the impact of the negative phase shift caused by the current regulator becomes less, so the upper boundary of H_{i1} rises first. But when f_c keeps increasing, the negative phase shift caused by the active-damping becomes larger and the dominate factor, the upper boundary of H_{i1} falls then.

It is noticed that, if the confirmed specifications of T_{fo}, PM, and GM determined in Step (1) are too strict, the satisfactory region may be very small or even does not exist. If that, return to Step (1) and modify the specifications and then renew Step (2).

Step 3) Determine f_c according to the satisfactory region constrained by the specifications aformentioned.

With the precondition of f_c lower than $f_s/5$ considering the attenuation of high-frequency noise, a larger f_c in the satisfactory region is preferred and then K_p from (9) is calculated.

Step 4) For a specific f_c, calculate the lower boundary of H_{i1} from (24), the upper boundaries of H_{i1} from (22) and (25), respectively. Then pick out a proper H_{i1} from this interval.

For a specific f_c, a larger H_{i1} leads to less PM and thus worse dynamic response with no T_{fo} increased, and thus cannot reduce the steady-state error. Therefore, it should be pointed out that there is no need to design a system that is overdamped or critically damped, which may lead to a poor dynamic response. A smaller H_{i1} in the satisfactory interval which offers enough GM is recommended.

Step 5) After f_c and H_{i1} have been determined, calculate the lower and upper boundaries of K_i from (18) and (21), respectively, and then picked out K_i from this interval.

For a specific f_c, a larger K_i leads to smaller steady-state error but less PM and thus worse dynamic response. Therefore, choose K_i from this interval by trading OFF between the steady-state error and PM of the system.

Step 6) Check the compensated system to ensure that all the specifications are well satisfied.

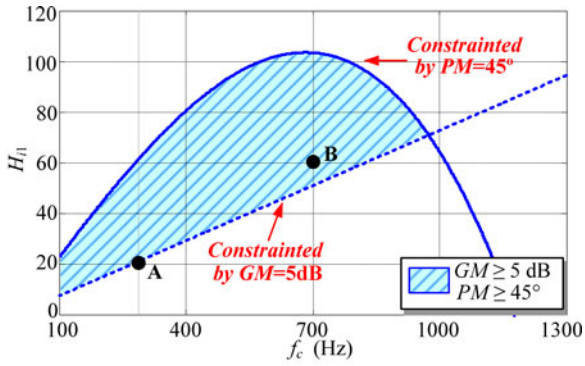

Fig. 6. Region of f_c and H_{i1} according to the parameters proposed in [24].

E. Controller Optimization and Robustness Analysis

According to (21), (22), (24), and (25), when PM $= 0^\circ$ and GM $= 0$ dB, respectively, the critical stability boudaries of K_i and H_{i1} can be obtained. If the chosen H_{i1} and K_i are outside these critical boudaries, the system will not have enough PM or GM to retain a stable operation. So we need to pay close attention to these critical boundaries when designing the controller parameters.

And it is noticed that, the satisfactory region plotted with the proposed design method is an effective design tool not only to choose but also to optimize the controller parameters whatever system parameters and design goals are. For instance, the satisfactory region according to the system parameters given in [24] is depicted in Fig. 6. In [24], in order to achieve a sufficiently damped frequency response at the f_r of the *LCL* filter while maintaining an acceptable phase margin, the controller

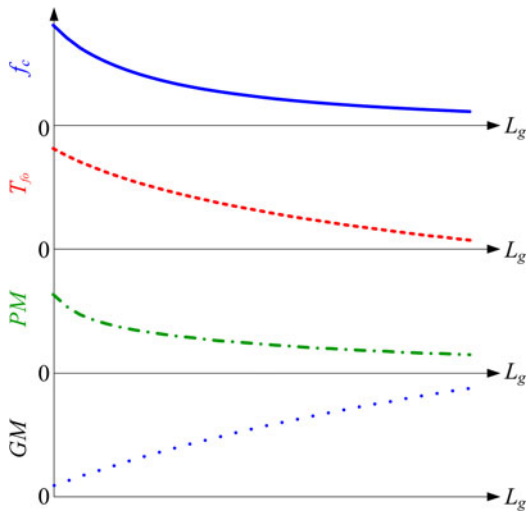

Fig. 7. Variation tendencies of f_c, T_{fo}, PM, and GM when L_g increases.

parameters at point A in Fig. 6 are chosen by authors based on root locus. According to the proposed design method and Fig. 6, it is intuitive and easy to pick out a group of controller parameters, for instance at point B, so that the compensated system has similar stability margin and a larger f_c which implies faster transient response (although the controller parameters at point B can also be achieved by proper parameters adjustment according to the design procedure proposed in [24]).

Furthermore, with the regions of H_{i1} and K_i obtained from the aforementioned design procedure, once f_c is determined, the controller parameters can be further optimized according to different requirements:

1) a larger K_i can be chosen to get a smaller steady-state error;
2) a larger H_{i1} can be chosen for a larger gain margin;
3) a smaller K_i and H_{i1} can be chosen for a larger phase margin.

The robustness of the system should also be respected. Although the specifications of the system, specifically, the PM and GM, have considered the robustness against the variations of the *LCL* filter parameters, in practical, the wide variation range of the grid impedance which does affect the properties of the system must be considered [4]. As the grid-side inductor L_2 is in series with the grid, the grid impedance L_g which is mainly inductive can be considered as a part of L_2. It is clear that, when L_g increases, f_c and T_{fo} decrease and thus the impact of the negative phase shift caused by the PI compensator becomes larger as f_c decreases, which leads to less PM. Besides, the increased L_g leads to larger GM. The variation tendencies of system specifications, i.e., f_c, T_{fo}, PM, and GM, in front of L_g variation are depicted in Fig. 7.

As f_c, T_{fo}, and PM all decrease when L_g increases, the steady-state and transient responses of the system will be inevitably worse. In order to obtain a better system performance in front of L_g variation, a larger K_p which leads to larger f_c and T_{fo}, and a smaller H_{i1} which leads to larger PM are welcomed. Therefore, choosing the upper boundary of K_p and lower boundary of H_{i1} introduced in Section IV-D, is preferred in this situation (and the choice of K_i should tradeoff between the steady-state response and transient response of the system).

V. Extension of the Proposed Design Method

In practical applications, in order to reduce the steady-state error of the injected grid current for the single-phase grid-connected inverter, PI compensator with the grid voltage feedforward scheme, and PR injected grid current regulator, are usually adopted. The controller design method proposed in Section IV is extended to these cases in this section.

A. Controller Design Based on PI Compensator With the Grid Voltage Feedforward Scheme

PI compensator is widely used for its simplicity and effectiveness, but it cannot achieve zero steady-state error of the injected grid current for a single-phase grid-connected inverter. An effective approach to reduce the steady-state error of the injected grid current is to feedforward the grid voltage [33], [43], [44]. It was pointed out in [43] that, for an *LCL*-type single-phase grid-connected inverter, when the grid voltage was feedforwarded, the component of the injected grid current i_{g2} produced by the grid voltage could be eliminated, thus the steady-state error was effectively reduced.

Therefore, E_A is the only steady-state error that should be considered, and the constraint of T_{fo} is determined by the current reference tracking. Since i_{g2} is eliminated, $I_g = I_{g1}, E_A$ can be redefined as

$$E_A \approx \frac{I_{\text{ref}} - H_{i2} I_{g1}}{I_{\text{ref}}} = 1 - \left| \frac{T(j2\pi f_o)}{1 + T(j2\pi f_o)} \right|. \tag{26}$$

As T_{fo} is much larger than 1, E_A can be approximated as

$$E_A \approx \frac{1}{|1 + T(j2\pi f_o)|} \approx \frac{1}{|T(j2\pi f_o)|} = 10^{-\frac{T_{fo}}{20}}. \tag{27}$$

Therefore, the minimum value of T_{fo} can be determined as $20\log_{10}(1/E_A)$. Since the grid voltage feedforward scheme has no effect on the loop gain, the controller design method proposed in Section IV can be extended to PI compensator plus the grid voltage feedforward control strategy without any other modification. The detail design procedure is not repeated here.

B. Controller Design Based on PR Compensator

Compared with PI compensator, PR compensator can provide larger gain at the fundamental frequency to eliminate the steady-sate error [27], [30], [31]. A practical transfer function of PR compensator is given by

$$G_i(s) = K_p + \frac{2K_r \omega_i s}{s^2 + 2\omega_i s + \omega_o^2} \tag{28}$$

where $\omega_o = 2\pi f_o$ and ω_i is the bandwidth of the resonant part concerning -3 dB cutoff frequency to reduce the sensitivity of the compensator to variations at the fundamental frequency, which means the gain of the resonant part of PR compensator is $K_r/\sqrt{2}$ at $\omega_o \pm \omega_i$. For small PV power stations, the

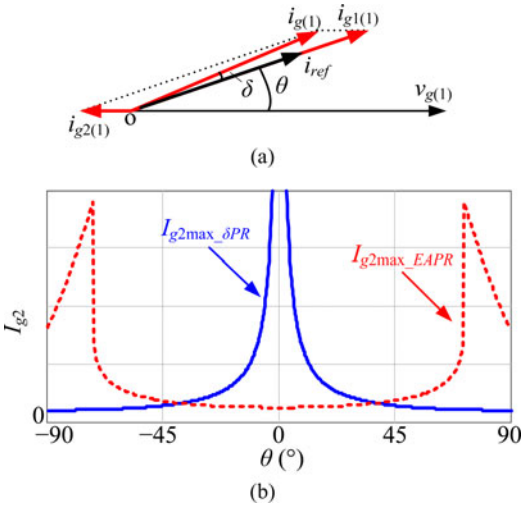

Fig. 8. Steady-state error with PR compensator. (a) Phasor diagrams of $i_{g(1)}, i_{g1(1)}, i_{g2(1)}, v_{g(1)}$, and $i_{\rm ref}$. (b) Variations of $I_{g2\max\_\rm EAPR}$, $I_{g2\max\_\delta\rm PR}$ for given E_A and δ when θ varies.

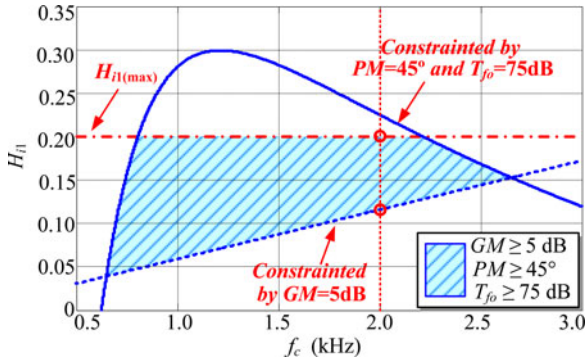

Fig. 9. Region of f_c and H_{i1} constrained by GM, PM, and T_{fo} with PR compensator.

grid-connected inverters are required to work normally when the fundamental frequency of the grid fluctuates between 49.5 and 50.2 Hz [42]. The corresponding maximum frequency fluctuation $\Delta f = 0.5$ Hz. Therefore, $\omega_i = 2\pi\Delta f = \pi$ rad/s is set to attain enough gain in the entire working frequency range.

According to (28), the bode diagram of PR compensator is depicted in Fig. 3. PR compensator can provide large gain at f_o, but it also introduces negative phase shift at the frequencies higher than the selected frequency, especially at the frequencies close to the selected resonance frequency, which damages the PM of the system. To avoid this side effect, the crossover frequency f_c is suggested to be set far away from the selected resonance frequency [4]. Therefore, PR compensator can be approximated to K_p in magnitude at f_c and the frequencies higher than f_c, which is similar to PI compensator. Thus, (9), (24), and (25) are still reasonable, that is to say, K_p can be expressed as the function of f_c given by (9), and H_{i1} is constrained by the functions of GM given by (24), and PWM constraint given by (25).

Different from the case that PI compensator is used, referring to (28) $G_i(j2\pi f_o) = K_p + K_r$ when PR compensator is adopted, so $i_{g2(1)} \approx -v_{g(1)}/[H_{i2}G_{\rm inv}(K_p + K_r)]$ according to (10). Therefore, $i_{g2(1)}$ is about 180° lagging behind $v_{g(1)}$, as shown in Fig. 8(a). Similar to the derivation depicted in Section IV-A, referring to Fig. 8(a) the upper boundaries of I_{g2} can be derived as

$$I_{g2\max\_\rm EAPR} \approx \begin{cases} \dfrac{I_{\rm ref}}{H_{i2}}\left(\cos\theta + \sqrt{(E_A+1)^2 - \sin^2\theta}\right) \\ \quad -90^\circ \le \theta < -\theta_2, \theta_2 < \theta \le 90^\circ \\ \dfrac{I_{\rm ref}}{H_{i2}}\left(\cos\theta - \sqrt{(E_A-1)^2 - \sin^2\theta}\right) \\ \quad -\theta_2 \le \theta \le \theta_2 \end{cases} \tag{29a}$$

$$I_{g2\_\delta\rm PR} \approx \frac{I_{\rm ref}}{H_{i2}}\left|\frac{\sin\delta}{\sin(\theta+\delta)}\right| \tag{29b}$$

where $\theta_2 = \arccos\sqrt{2E_A - E_A^2}$, $I_{g2\max\_\rm EAPR}$, and $I_{g2\max\_\delta\rm PR}$ are the upper boundaries of I_{g2} constrained by E_A and δ, respectively, and $\delta = 0$ when $\theta = 0°$.

According to (29), the variations of $I_{g2\max\_\rm EAPR}$ and $I_{g2\max\_\delta\rm PR}$ when θ varies are depicted as Fig. 8(b). As E_A and δ should be small for a properly designed inverter, as seen, $I_{g2\max\_\rm EAPR}$ is minimum when $\theta \approx 0°$ and $I_{g2\max\_\delta\rm PR}$ is minimum when $\theta \approx \pm 90°$. Thus, when PR compensator is used, the specific requirement of the steady-state error can be simplified to the requirement of $\min\{I_{g2\max\_\rm EAPR}, I_{g2\max\_\delta\rm PR}\}$, and then this requirement can also be further specified by the requirement of T_{fo} according to (16).

As the gain of the resonant part of the PR compensator is $K_r/\sqrt{2}$ at $f_o \pm \Delta f$, thus $\sqrt{2}$ times of the gain in magnitude at f_o are required to ensure enough magnitude of the loop gain when the fundamental frequency fluctuates between $f_o \pm \Delta f$. Therefore, considering (7), (9), and (28), K_r can be derived as

$$K_r = \left(\sqrt{2}10^{\frac{T_{fo}}{20}} f_o - f_c\right)\frac{2\pi(L_1+L_2)}{H_{i2}G_{\rm inv}}. \tag{30}$$

According to (19) and (28), the PM can be rewritten as

$$\rm PM = \arctan\frac{2\pi L_1\left(f_r^2 - f_c^2\right)}{H_{i1}G_{\rm inv}f_c} - \arctan\frac{K_r\omega_i}{\pi f_c K_p} \tag{31}$$

where $G_i(s)$ is approximated as $K_p + 2K_r\omega_i/s$ at f_c, for f_c is much larger than f_o and ω_i/π.

According to (31), K_r can also be expressed as

$$K_r = \frac{\pi f_c K_p}{\omega_i}\frac{2\pi L_1\left(f_r^2 - f_c^2\right) - H_{i1}G_{\rm inv}f_c\tan\rm PM}{H_{i1}G_{\rm inv}f_c + 2\pi L_1\left(f_r^2 - f_c^2\right)\tan\rm PM}. \tag{32}$$

Substituting (9) and (30) into (32) leads to the expression of H_{i1}, given by

$$H_{i1} = \frac{2\pi L_1\left(f_r^2 - f_c^2\right)}{G_{\rm inv}f_c}\frac{\pi f_c^2 - \left(\sqrt{2}10^{\frac{T_{fo}}{20}} f_o - f_c\right)\omega_i\tan\rm PM}{\left(\sqrt{2}10^{\frac{T_{fo}}{20}} f_o - f_c\right)\omega_i + \pi f_c^2\tan\rm PM}. \tag{33}$$

Based on (24), (25), and (33), the possible H_{i1} and f_c that satisfy the specifications of T_{fo}, GM, and PM are included in the shaded area depicted in Fig. 9. It is noticed that the characteristics of the controller parameters based on PR compensator are almost the same as that based on PI compensator, except K_i

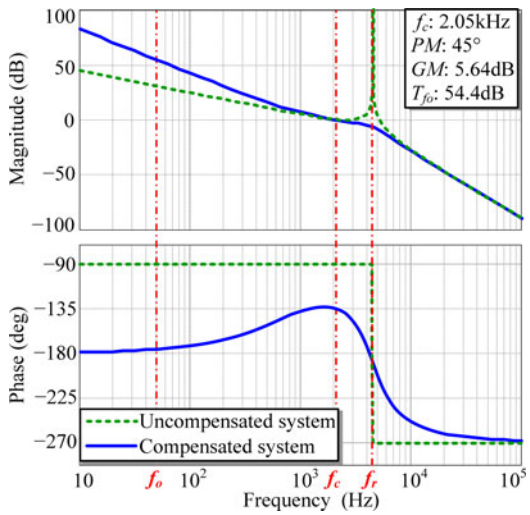

Fig. 10. Bode diagram of the compensated system with PI compensator.

is replaced by K_r. Therefore, the design procedure proposed in Section IV-D can be extended to this case, except (18), (21), (22) are replaced by (30), (32), (33), respectively, and the optimized design of the controller parameters and analysis of system robustness proposed in Section IV-E are also applicable in the PR case.

VI. Design Example and Simulation Results

A design example of the PI injected grid current regulator and capacitor–current-feedback active-damping for an *LCL*-type single-phase grid-connected inverter is presented in this section. The key parameters of the inverter are given in Table I.

First, the specifications of the loop gain are given as follows: PM $\geq 45^\circ$ and GM ≥ 5 dB, which ensure good dynamic performance and enough stability margin; $T_{fo} \geq 52$ dB, which ensures PF greater than 0.98 when the output power of the inverter is larger than 50% of the rated power [42], so the corresponding PF is greater than 0.994 and amplitude error is less than 0.5% at the rated power.

Then the satisfactory region of H_{i1} and f_c constrained by the aforementioned specifications is calculate according to (22), (24), and (25), as depicted in Fig. 5. Based on this satisfactory region, the crossover frequency f_c is set at 2 kHz (1/5 switching frequency of the inverter) here to ensure that the system has fast dynamic response and good ability of attenuating high-frequency noise. After that, $K_p = 0.45$ is calculated from (9). Substituting $f_c = 2$ kHz into (22), (24) and (25), the possible interval of H_{i1}, which is (0.114, 0.165), can be obtained. To get larger phase margin, $H_{i1} = 0.12$ is chosen. Substituting $f_c = 2$ kHz and $H_{i1} = 0.12$ into (18) and (21), the possible interval of K_i, which is (1657, 2205), can be obtained. By trading off between the steady-state error and phase margin, $K_i = 2200$ is chosen to get better steady-state response.

Afterward, the bode diagram of the loop gain with compensation is depicted in Fig. 10, the crossover frequency of the compensated loop gain is 2.05 kHz, the PM is 45°, the GM is 5.6 dB, and the gain in magnitude at the fundamental frequency is 54.4 dB. It is obvious that all the specifications are satisfied as expected.

To examine the robustness of the system, the bode diagrams of the compensated loop gain considering the variations of the *LCL* filter parameters are given in Fig. 11. The grid impedance L_g is considered as a part of L_2. It is found that, although C varies from 8 to 12 μF (10 μF $\pm$ 20%), L_1 varies from 480 to 720 μH (600 μH $\pm$ 20%), or L_2 varies from 100 to 600 μH (150 μH – 30% + 300%, considering the effect of the grid impedance), the lowest crossover frequency is still higher than 1.3 kHz, the PM is larger than 24°, the GM is larger than 5 dB, and the gain in magnitude at the fundamental frequency is larger than 51 dB. All of these results verify that the designed system has a strong robustness, which is in accordance with the analysis in Section IV-E.

Fig. 12 shows the simulation results with the controller parameters designed above. Fig. 12(a) shows the steady-state waveform of the compensated system at full load, the power factor is 0.997, and the fundamental rms value of i_g is 27.38 A (the reference value is 27.27 A), thus the amplitude error is 0.4%. Fig. 12(b) shows the transient response of the compensated system. As the current regulator may be saturated when the reference value $i_{\rm ref}$ steps up from half load to full load, here the transient response of the inverter when $i_{\rm ref}$ steps down from full load to half load is measured, the percentage overshoot (PO) of i_g [$\sigma/I_{\rm step}$ in Fig. 12(b)] is 45.2%, and the settling time is about 1.2 ms.

With the same system parameters given in Table I, when PR compensator is adopted, the specifications of the loop gain are given as follows: $T_{fo} \geq 75$ dB ensuring the amplitude error less than 1% at the rated power ($I_{g2\max\_\rm EAPR}$ is minimum when $\theta = 0^\circ$, and the PFs constrained by [41], [42] are easy to be satisfied), and PM $\geq 45^\circ$, GM ≥ 5 dB. With the assistance of the satisfactory parameter region depicted in Fig. 9, the PR compensator and capacitor–current feedback coefficient can be easily chosen as $K_p = 0.45$, $K_r = 350$, $H_{i1} = 0.12$. The bode diagram of the compensated loop gain is depicted in Fig. 13. Fig. 14 shows the simulation results of the compensated system, the power factor is 1.0, the fundamental rms value of i_g is 27.2 A, the amplitude error is 0.3%, and PO is 45%, the settling time is about 1.2 ms. The design and simulation results verify the effectiveness of the proposed simple frequency-based design method.

VII. Experimental Results

A 6-kW prototype has been constructed in the lab to verify the analysis given above and the effectiveness of the proposed step-by-step design method. The parameters of the prototype are listed in Table I. A galvanic isolated transformer is placed between the single-phase grid-connected inverter and the grid, and the leakage inductor of the transformer is included in L_2. The grid-connected inverter is implemented using two insulated gate bipolar transistor modules (CM100DY- 24NF). These modules are driven by M57962L. The grid voltage is sensed by a hall voltage transducer (LV25-P) for the PLL. The filter capacitor

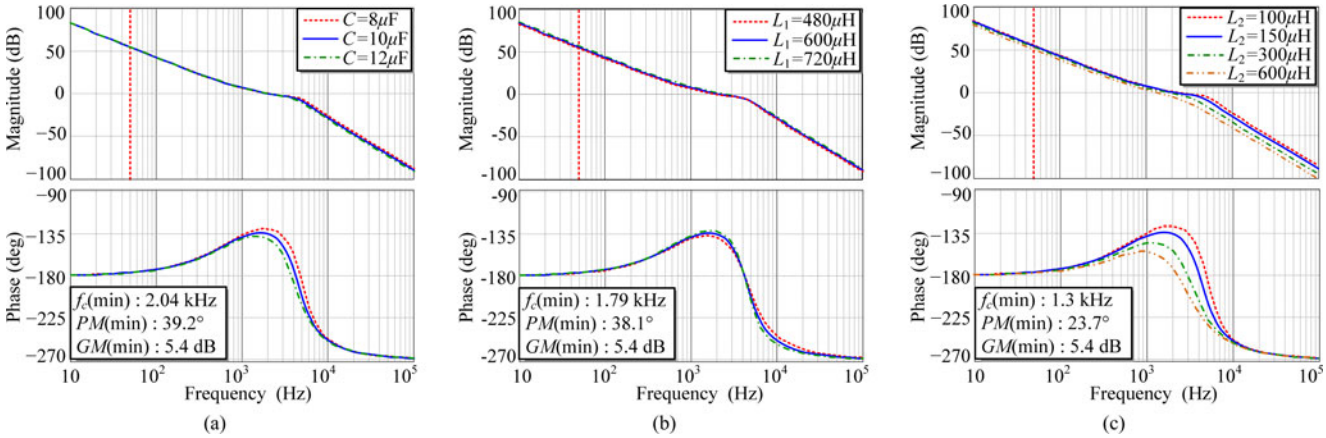

Fig. 11. Bode diagrams of system considering the variations of the *LCL* filter parameters. (a) C varies from 8 to 12 μF (10 μF $\pm$ 20%). (b) L_1 varies from 480 to 720 μH (600 μH $\pm$ 20%). (c) L_2 varies from 100 to 600 μH (150 μH – 30% + 300%).

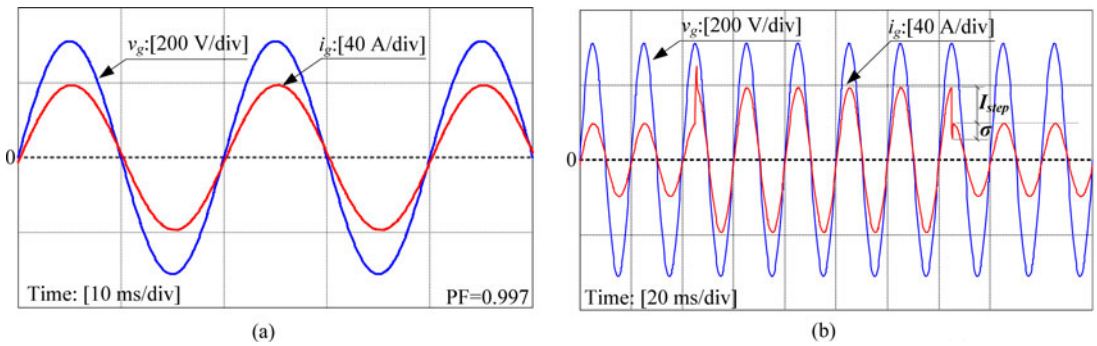

Fig. 12. Simulation results ($H_{i1} = 0.12$, $K_p = 0.45$, $K_i = 2200$). (a) Steady-state response. (b) When the reference of i_g jumps between half and full load.

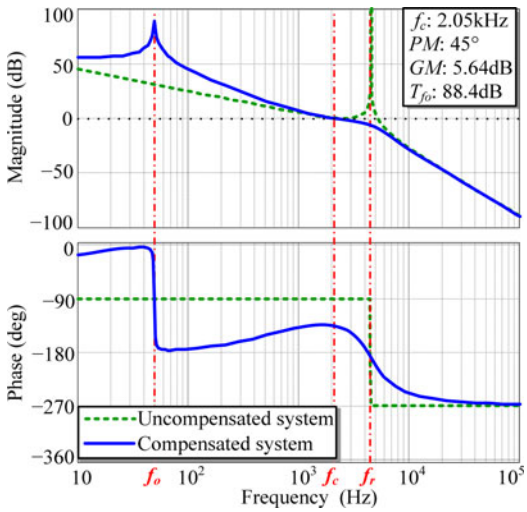

Fig. 13. Bode diagram of the compensated system with PR compensator.

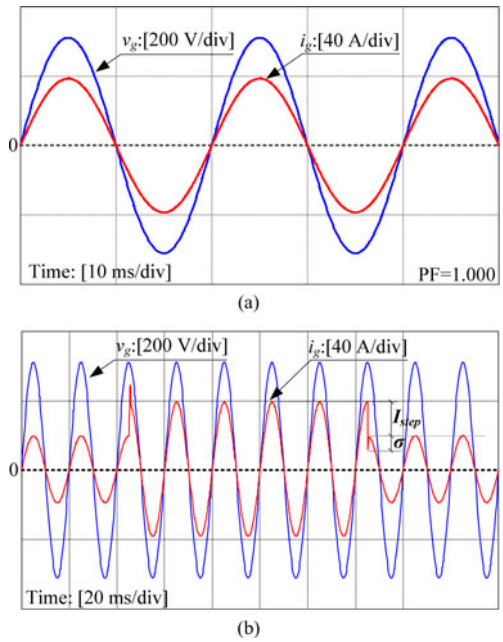

Fig. 14. Simulation results ($H_{i1} = 0.12$, $K_p = 0.45$, $K_r = 350$). (a) Steady-state response. (b) When the reference of i_g jumps between half and full load.

current and injected grid current are sensed by two hall current transducers (LA55-P). TL074 is used to implement both PI and PR compensators, ICL8038 is used to generate the analog triangle carrier wave, and LM311 is used to compare the carrier and modulation waves.

Fig. 15 shows the experimental waveforms when PI compensator is used as the injected grid current regulator. Fig. 15(a) shows the experimental waveform at full load, the measured power factor is 0.995, and the fundamental rms value of i_g is

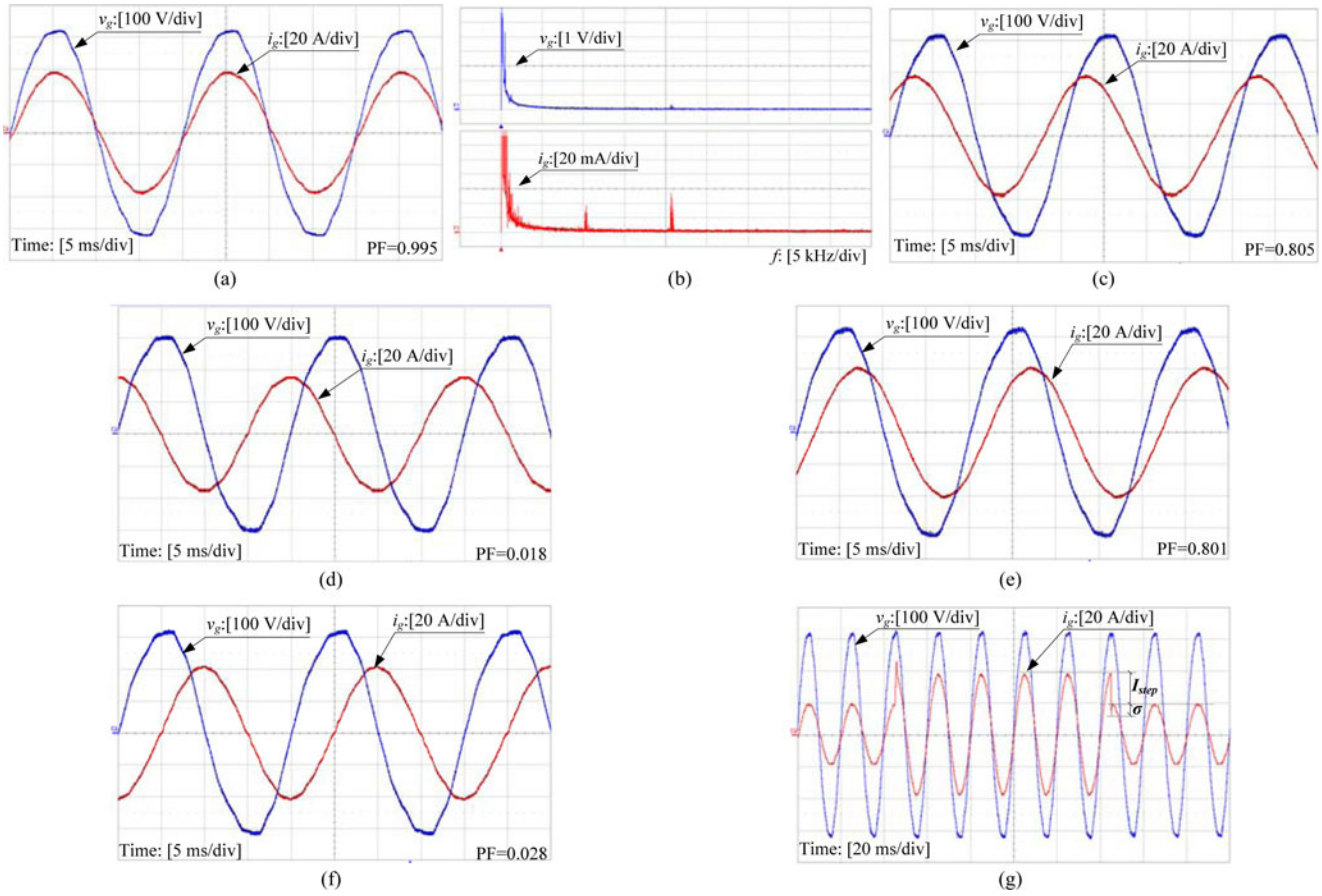

Fig. 15. Experimental waveforms with PI compensator ($H_{i1} = 0.12$, $K_p = 0.45$, $K_i = 2200$) when PFs of the system are set to (a) 1.0 and (b) its corresponding spectrum of v_g and i_g, (c) 0.8 (capacitive), (d) 0 (capacitive), (e) 0.8 (inductive), and (f) 0 (inductive), respectively. (g) Injected grid current reference jumps between half and full load with PF set to 1.0.

TABLE II
STEADY-STATE ERRORS OF THE EXPERIMENT RESULTS

PF of the reference	Measured PF of i_g		δ (°)		Measured fundamental RMS value of i_g (A)		E_A	
	PI	PR	PI	PR	PI	PR	PI	PR
1.0	0.995	0.999	5.73	2.56	27.13	27.1	0.005	0.006
0.8 capacitive	0.805	0.776	0.48	2.23	26.11	27.26	0.042	0.001
0 capacitive	0.018	−0.028	1.03	1.60	25.18	27.29	0.076	0.001
0.8 inductive	0.801	0.820	0.10	1.95	28.39	27.26	0.041	0.001
0 inductive	0.028	−0.019	1.6	1.09	28.98	27.29	0.063	0.001

27.13 A, the amplitude error is 0.5%. Fig. 15(b) shows the spectra of v_g and i_g. Because of the dead-time effect, i_g contains harmonics at f_s, and the frequencies nearby, but the switching harmonics are all less than 0.3% of the fundamental current at rated power. The attenuation of switching harmonics satisfies the specified requirements of the *LCL* filter. Figs. 15(c)–(f) show the experimental waveforms at full load when the PFs of the system are set to 0.8 (capacitive), 0 (capacitive), 0.8 (inductive), and 0 (inductive), respectively, and the steady-state errors are listed in Table II. Fig. 15(g) shows the experimental waveform when the reference value of the injected grid current step changes between half load and full load. The measured PO of i_g [$\sigma/I_{\rm step}$ in Fig. 15(g)] is 38% and the settling time is about 1.5 ms.

Fig. 16 shows the experimental waveforms when PR compensator is used as the injected grid current regulator. Fig. 16(a) shows the experimental waveform at full load, the measured power factor is 0.999, the fundamental rms value of i_g is 27.1 A, the amplitude error is 0.6%. Figs. 16(b)–(e) show the experimental waveforms at full load when the PFs of the reference are nonunity, the steady-state errors are listed in Table II. From Fig. 16(f), the measured PO of i_g [$\sigma/I_{\rm step}$ in Fig. 16(f)] is 38%, and the settling time is about 1.5 ms. Compared with the experimental waveforms when PI compensator is used, the system with PR compensator has similar responses except the amplitude errors are much smaller especially when the PFs of the reference decrease.

Because of the measurement error, and the effect of the dead time, parasitic parameters, grid voltage distortion, etc., the steady-state errors of the experiment results are a bit larger than the simulation results and the transient responses are better than the simulation results. All the experiment waveforms verify the effectiveness of the proposed design method.

Taking PI compensator for instance, Fig. 17 shows the diagrams of the measured amplitude error, power factor, and

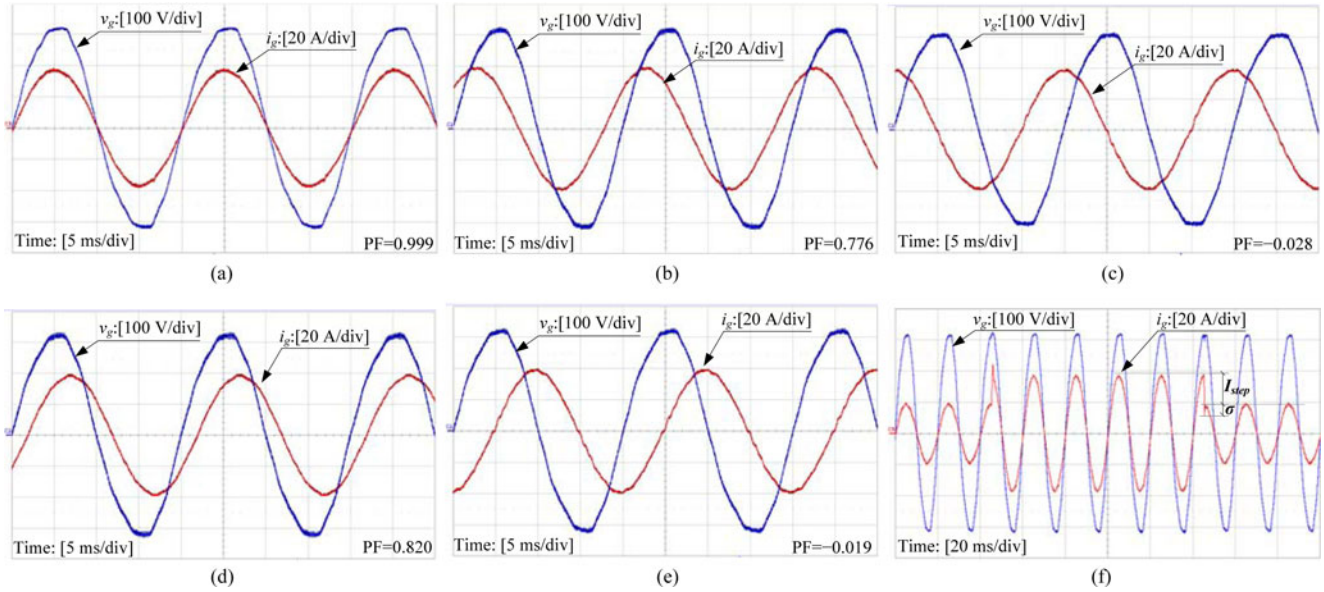

Fig. 16. Experimental waveforms with PR compensator ($H_{i1} = 0.12$, $K_p = 0.45$, $K_r = 350$) when PFs of the system are set to (a) 1.0, (b) 0.8 (capacitive), (c) 0 (capacitive), (d) 0.8(inductive), and (e) 0 (inductive), respectively. (f) Injected grid current reference jumps between half and full load with PF set to 1.0.

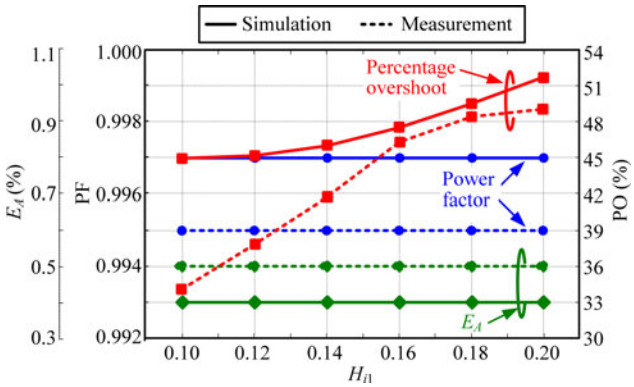

Fig. 17. Amplitude error, power factor, and percentage overshoot of i_g when H_{i1} varies ($K_p = 0.45$, $K_i = 2200$).

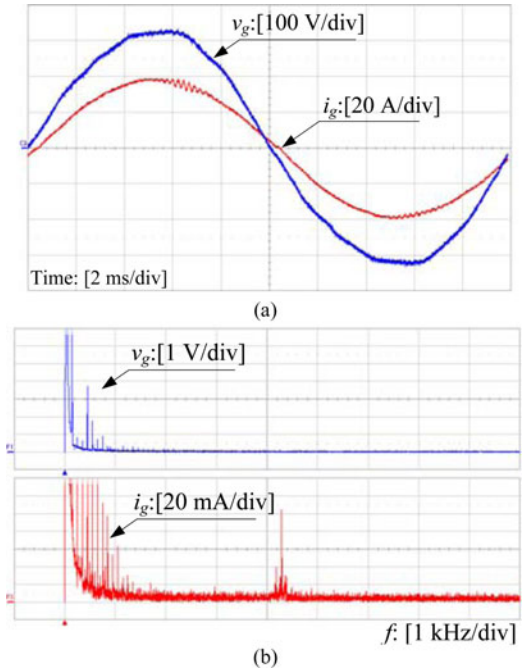

Fig. 18. Oscillation of experimental results at full load ($H_{i1} = 0.016$, $K_p = 0.45$, $K_i = 2200$). (a) Experimental waveform. (b) Spectra of v_g and i_g.

percentage overshoot of i_g at rated power when H_{i1} varies. When H_{i1} increases from 0.1 to 0.2, the experimentally measured PO increases from 34% to 50%, the amplitude error keeps 0.5%, and the power factor keeps 0.995. It is obvious that, increasing H_{i1} has no improvement in steady-state error, but it reduces the PM and thus increases the percentage overshoot. Fig. 18 shows the experimental waveforms when H_{i1} is reduced to 0.016, from which it can be seen that there is resonance oscillation at the frequency near f_r in the output current. This means that a too small H_{i1} will result in resonance oscillation and even instability of the system. The experimental results are in accordance with the analysis in Section IV that a small H_{i1} in the satisfactory region will lead to good dynamic performance with no impact on the steady-state response, and H_{i1} outside the stability boundary cannot be tolerated.

Fig. 19 shows the diagram of the measured amplitude error, power factor, and percentage overshoot of i_g at rated power when K_i increases from 600 to 2600. It can be seen that the measured amplitude error decreases from 5.8% to 0.5%, the power factor increases from 0.935 to 0.996, and the percentage overshoot increases from 11% to 41%. There is significant improvement in the steady-state error when K_i increases, but the PM decreases and the percentage overshoot increases as well. However, a too large K_i leads to resonance oscillation of the output current at the frequency near the bandwidth frequency or even unstable response, as shown in Fig. 20. The results are in accordance with the analysis of K_i in Section IV and the appropriate K_i could be picked out from the satisfactory interval by trading off between the steady-state error and the PM of the system.

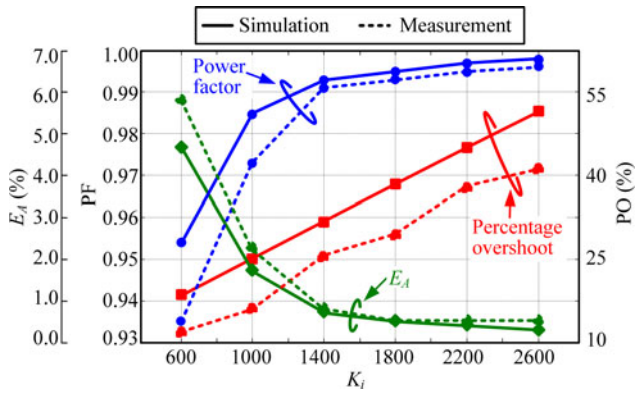

Fig. 19. Amplitude error, power factor, and percentage overshoot of i_g when K_i varies ($H_{i1} = 0.12$, $K_p = 0.45$).

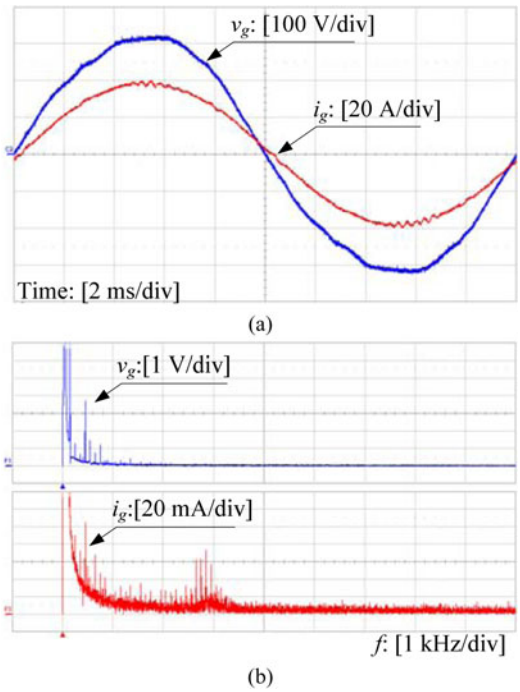

Fig. 20. Oscillation of experimental results at full load ($H_{i1} = 0.12$, $K_p = 0.45$, $K_i = 7400$). (a) Experimental waveform. (b) Spectra of v_g and i_g.

VIII. Conclusion

This paper has studied the characteristics and design method of the injected grid current regulator and capacitor–current-feedback active-damping for the *LCL*-type grid-connected inverter. The relationship between the controller parameters and the system loop gain has been investigated: 1) active-damping method based on the feedback of the filter capacitor current can damp the resonance peak caused by the *LCL* filter effectively, but it impairs the PM of the system; 2) the injected grid current regulator determines the crossover frequency and steady-state error of the system, but the negative phase shift of the regulator impairs the phase margin. A proper simple step-by-step interactive and optimized controller design method is proposed in this paper. The satisfactory regions of the controller parameters constrained by the specifications of the phase margin, gain margin, and steady-state error, are calculated and drawn to assist in determining and optimizing the controller parameters. Thus the compensated system can satisfy all the aforementioned specifications. Experimental results of a 6-kW prototype verify the effectiveness of the proposed design method and validity of the analysis. This idea has been investigated based on PI current regulator in detail, and extended to the controller design based on PI current regulator plus grid voltage feedforward scheme, PR current regulator, and also can be applied to the controller design of *LCL*-type three-phase grid-connected inverters. It is hoped that this work will offer a useful reference for engineers to design the controller parameters of *LCL*-type grid-connected inverters.

Appendix

The upper boundary of I_{g2} constrained by E_A when PI compensator is used, $I_{g2\max\_\mathrm{EAPI}}$, is derived in this Appendix. For a properly designed inverter, I_{g2} is small and $E_A \ll 1$, thus (11) can be rewritten as

$$\pm E_A = \frac{H_{i2}}{I_{\mathrm{ref}}}\sqrt{I_{g1}^2 + I_{g2}^2 - 2I_{g1}I_{g2}\sin\theta} - 1. \tag{A.1}$$

As $i_{g1(1)} \approx i_{\mathrm{ref}}/H_{i2}$ thus $I_{g1} \approx I_{\mathrm{ref}}/H_{i2}$, solving (A.1), the roots of I_{g2} can be expressed as

$$\begin{aligned}
I_{g2_rt1} &= \frac{I_{\mathrm{ref}}}{H_{i2}}\left(\sin\theta + \sqrt{\sin^2\theta - 2E_A + E_A^2}\right)\\
I_{g2_rt2} &= \frac{I_{\mathrm{ref}}}{H_{i2}}\left(\sin\theta - \sqrt{\sin^2\theta - 2E_A + E_A^2}\right)\\
I_{g2_rt3} &= \frac{I_{\mathrm{ref}}}{H_{i2}}\left(\sin\theta + \sqrt{\sin^2\theta + 2E_A + E_A^2}\right)\\
I_{g2_rt4} &= \frac{I_{\mathrm{ref}}}{H_{i2}}\left(\sin\theta - \sqrt{\sin^2\theta + 2E_A + E_A^2}\right).
\end{aligned} \tag{A.2}$$

As $I_{g2} \geq 0$ and $I_{g2\_rt4} < 0$, the root I_{g2_rt4} is invalid.

If $-90° \leq \theta \leq -\theta_1$ where $\theta_1 = \arcsin\sqrt{2E_A - E_A^2}$, both I_{g2_rt1} and I_{g2_rt2} are negative and invalid and $I_{g2\max\_\mathrm{EAPI}}$ is given as

$$\begin{aligned}
I_{g2\max_\mathrm{EAPI}} &= I_{g2_rt3}\\
&= \frac{I_{\mathrm{ref}}}{H_{i2}}\left(\sin\theta + \sqrt{\sin^2\theta + 2E_A + E_A^2}\right).
\end{aligned} \tag{A.3}$$

If $-\theta 1 < \theta < \theta_1, \sin^2\theta - 2E_A + E_A^2 < 0$, and I_{g2_rt1} and I_{g2_rt2} are inexistent, $I_{g2\max\_\mathrm{EAPI}}$ is given as

$$I_{g2\max\_\mathrm{EAPI}} = I_{g2\_rt3} = \frac{I_{\mathrm{ref}}}{H_{i2}}\left(\sin\theta + \sqrt{\sin^2\theta + 2E_A + E_A^2}\right). \tag{A.4}$$

Else if $\theta_1 \leq \theta \leq -90°$, I_{g2_rt1}, I_{g2_rt2}, and I_{g2_rt3} are all valid. Choose the smallest root as $I_{g2\max\_\mathrm{EAPI}}$, given as

$$I_{g2\max\_\mathrm{EAPI}} = I_{g2\_rt2} = \frac{I_{\mathrm{ref}}}{H_{i2}}\left(\sin\theta - \sqrt{\sin^2\theta - 2E_A + E_A^2}\right). \tag{A.5}$$

Therefore, $I_{g2\max\_\mathrm{EAPI}}$ can be expressed as

$$I_{g2\max\_\mathrm{EAPI}} \approx \begin{cases} \dfrac{I_{\mathrm{ref}}}{H_{i2}}\left(\sin\theta + \sqrt{(E_A+1)^2 - \cos^2\theta}\right) \\ \quad -90^\circ \le \theta < \theta_1 \\ \dfrac{I_{\mathrm{ref}}}{H_{i2}}\left(\sin\theta - \sqrt{(E_A-1)^2 - \cos^2\theta}\right) \\ \quad \theta_1 \le \theta \le 90^\circ. \end{cases} \tag{A.6}$$

REFERENCES

[1] F. Blaabjerg, R. Teodorescu, M. Liserre, and A. Timbus, "Overview of control and grid synchronization for distributed power generation systems," *IEEE Trans. Ind. Electron.*, vol. 53, no. 5, pp. 1398–1409, Oct. 2006.

[2] M. Lindgren and J. Svensson, "Control of a voltage-source converter connected to the grid through an *LCL*-filter-application to active filtering," in *Proc. IEEE Power Electron. Spec. Conf.*, 1998, pp. 229–235.

[3] A. Hava, T. Lipo, and W. L. Erdman, "Utility interface issues for line connected PWM voltage source converters: A comparative study," in *Proc. IEEE Appl. Power Electron. Conf.*, 1995, pp. 125–132.

[4] M. Liserre, R. Teodorescu, and F. Blaabjerg, "Stability of photovoltaic and wind turbine grid-connected inverters for a large set of grid impedance values," *IEEE Trans. Power Electron.*, vol. 21, no. 1, pp. 263–272, Jan. 2006.

[5] M. Liserre, A. Dell'Aquila, and F. Blaabjerg, "Stability improvements of an *LCL*-filter based three-phase active rectifier," in *Proc. IEEE Power Electron. Spec. Conf.*, 2002, pp. 1195–1201.

[6] M. Liserre, F. Blaabjerg, and S. Hansen, "Design and control of an *LCL*-filter-based three-phase active rectifier," *IEEE Trans. Ind. Appl.*, vol. 41, no. 5, pp. 1281–1291, Sep./Oct. 2005.

[7] R. Peña-Alzola, M. Liserre, F. Blaabjerg, R. Sebastián, J. Dannehl, and F. W. Fuchs, "Analysis of the passive damping losses in *LCL*-filter-based grid converters," *IEEE Trans. Power Electron.*, vol. 28, no. 6, pp. 2642–2646, Jun. 2013.

[8] T. Wang, Z. Ye, G. Sinha, and X. Yuan, "Output filter design for a grid-interconnected three-phase inverter," in *Proc. IEEE Power Electron. Spec. Conf.*, 2003, pp. 779–784.

[9] R. W. Erickson and D. Maksimovic, *Fundamentals of Power Electronics*, 2nd ed. Norwell, MA, USA: Kluwer, 2001, pp. 331–408.

[10] P. A. Dahono, Y. R. Bahar, Y. Sato, and T. Kataoka, "Damping of transient oscillations on the output *LC* filter of PWM inverters by using a virtual resistor," in *Proc. IEEE Int. Conf. Power Electron. Drive Syst.*, 2001, pp. 403–407.

[11] V. Blasko and V. Kaura, "A novel control to actively damp resonance in input *LC* filter of a three-phase voltage source converter," *IEEE Trans. Ind. Appl.*, vol. 33, no. 2, pp. 542–550, Mar./Apr. 1997.

[12] J. Dannehl, M. Liserre, and F. W Fuchs, "Filter-based active damping of voltage source converters with *LCL*-filter," *IEEE Trans. Ind. Electron.*, vol. 58, no. 8, pp. 3623–3633, Aug. 2011.

[13] J. Dannehl, F. W. Fuchs, and P. B. Thøgersen, "PI state space current control of grid-connected PWM converters with *LCL* filters," *IEEE Trans. Power Electron.*, vol. 25, no. 9, pp. 2320–2330, Sep. 2010.

[14] E. Wu and P. Lehn, "Digital current control of a voltage source converter with active damping of *LCL* resonance," *IEEE Trans. Power Electron.*, vol. 21, no. 5, pp. 1364–1373, Sep. 2006.

[15] I. J. Gabe, V. F. Montagner, and H. Pinheiro, "Design and implementation of a robust current controller for VSI connected to the grid through an *LCL* filter," *IEEE Trans. Power Electron.*, vol. 24, no. 6, pp. 1444–1452, Jun. 2009.

[16] K. H. Ahmed, A. M. Massoud, S. J. Finney, and B. W. Williams, "A modified stationary reference frame-based predictive current control with zero steady-state error for *LCL* coupled inverter-based distributed generation systems," *IEEE Trans. Ind. Electron.*, vol. 58, no. 4, pp. 1359–1370, Apr. 2011.

[17] J. M. Espí, J. Castelló, R. García-Gil, G. Garcerá, and E. Figueres, "An adaptive robust predictive current control for three-phase grid-connected inverters," *IEEE Trans. Ind. Electron.*, vol. 58, no. 8, pp. 3537–3546, Aug. 2011.

[18] K. J. Lee, B. G. Park, R. Y. Kim, and D. S. Hyun, "Robust predictive current controller based on a disturbance estimator in a three-phase grid-connected inverter," *IEEE Trans. Power Electron.*, vol. 27, no. 1, pp. 276–283, Jan. 2012.

[19] J. C. Doyle, K. Glover, P. P. Khargonekar, and B. A. Francis, "State-space solutions to standard H2 and H∞ control problems," *IEEE Trans. Autom. Control*, vol. 34, no. 8, pp. 831–847, Aug. 1989.

[20] G. Willmann, D. F. Coutinho, L. F. A. Pereira, and F. B. Líbano, "Multiple-loop h-infinity control design for uninterruptible power supplies," *IEEE Trans. Ind. Electron.*, vol. 54, no. 3, pp. 1591–1602, Jun. 2007.

[21] T. Hornik and Q. Zhong, "A current-control strategy for voltage-source inverters in microgrids based on H∞ and repetitive control," *IEEE Trans. Power Electron.*, vol. 26, no. 3, pp. 943–952, Mar. 2011.

[22] S. Yang, Q. Lei, F. Z. Peng, and Z. Qian, "A robust control scheme for grid-connected voltage-source inverters," *IEEE Trans. Ind. Electron.*, vol. 58, no. 1, pp. 202–212, Jan. 2011.

[23] Q. Zhong and T. Hornik, "Cascaded current-voltage control to improve the power quality for a grid-connected inverter with a local load," *IEEE Trans. Ind. Electron.*, vol. 58, no. 1, pp. 202–212, Jan. 2011.

[24] E. Twining and D. G. Holmes, "Grid current regulation of a three-phase voltage source inverter with an *LCL* input filter," *IEEE Trans. Power Electron.*, vol. 18, no. 3, pp. 888–895, May 2003.

[25] Y. A.-R. I. Mohamed, "Suppression of low- and high-frequency instabilities and grid-induced disturbances in distributed generation inverters," *IEEE Trans. Power Electron.*, vol. 26, no. 12, pp. 3790–3803, Dec. 2011.

[26] J. Dannehl, F. W. Fuchs, S. Hansen, and P. B. Thgersen, "Investigation of active damping approaches for PI-based current control of grid-connected pulse width modulation converters with *LCL* filters," *IEEE Trans. Ind. Appl.*, vol. 46, no. 4, pp. 1509–1517, Jul./Aug. 2010.

[27] D. G. Holmes, T. A. Lipo, B. P. Mcgrath, and W. Y. Kong, "Optimized design of stationary frame three phase AC current regulators," *IEEE Trans. Power Electron.*, vol. 24, no. 11, pp. 2417–2426, Nov. 2009.

[28] F. Liu, Y. Zhou, S. Duan, J. Yin, B. Liu, and F. Liu, "Parameter design of a two-current-loop controller used in a grid-connected inverter system with *LCL* filter," *IEEE Trans. Ind. Electron.*, vol. 56, no. 11, pp. 4483–4491, Nov. 2009.

[29] J. Dannehl, C. Wessels, and F. W. Fuchs, "Limitations of voltage-oriented PI current control of grid-connected PWM rectifiers with *LCL* filters," *IEEE Trans. Ind. Electron.*, vol. 56, no. 2, pp. 380–388, Feb. 2009.

[30] G. Shen, X. Zhu, J. Zhang, and D. Xu, "A new feedback method for PR current control of *LCL*-filter-based grid-connected inverter," *IEEE Trans. Ind. Electron.*, vol. 57, no. 6, pp. 2033–2041, Jun. 2010.

[31] D. N. Zmood and D. G. Holmes, "Stationary frame current regulation of PWM inverters with zero steady-state error," *IEEE Trans. Power Electron.*, vol. 18, no. 3, pp. 814–822, May 2003.

[32] D. Younger, "A simple derivation of Mason's gain formula," *Proc. IEEE*, vol. 51, no. 7, pp. 1043–1044, Jul. 1963.

[33] T. Abeyasekera, C. Johnson, D. Atkinson, and M. Armstrong, "Suppression of line voltage related distortion in current controlled grid connected inverters," *IEEE Trans. Power Electron.*, vol. 20, no. 6, pp. 1393–1401, Nov. 2005.

[34] N. R. Zargari and G. Joos, "Performance investigation of a current-controlled voltage-regulated PWM rectifier in rotating and stationary frames," *IEEE Trans. Ind. Electron.*, vol. 42, no. 4, pp. 396–401, Aug. 1995.

[35] M. P. Kazmierkowski and L. Malesani, "Current control techniques for three-phase voltage-source PWM converters: a survey," *IEEE Trans. Ind. Electron.*, vol. 45, no. 5, pp. 691–703, Oct. 1998.

[36] D. N. Zmood, "A systematic development of improved linear regulators for sinusoidal power converters," Ph. D. dissertationthesis, Dept. Elect. Comput. Syst. Eng., Monash University, Victoria, Australia, 2002.

[37] M. P. Kazmierkowski, F. Blaabjerg, and R. Krishnan, *Control in Power Electronics—Selected Problems.* New York, NY, USA: Academic, 2002.

[38] S. Buso and P. Mattavelli, *Digital Control in Power Electronics*. Ft. Collins, Colorado, USA: Morgan & Claypool, 2006.

[39] F. O. Martinz, R. D. Miranda, W. Komatsu, and L. Matakas, "Gain limits for current loop controllers of single and three-phase PWM converters," in *Proc. IEEE Int. Power Electron. Conf.*, 2010, pp. 201–208.

[40] K. Jalili and S. Bernet, "Design of *LCL* filters of active-front-end two-level voltage-source converters," *IEEE Trans. Ind. Electron.*, vol. 56, no. 5, pp. 1674–1689, May 2009.

[41] *IEEE Recommended Practice for Utility Interface of Photovoltaic (PV) Systems*, IEEE Std. 929–2000, Jan. 2000.
[42] *Technical Rule for Photovoltaic Power Station Connected to Power Grid*, Q/GDW 617–2011, May 2011, (in Chinese).
[43] X. Wang, X. Ruan, S. Liu, and C. K. Tse, "Full feed-forward of grid voltage for grid-connected inverter with *LCL* filter to suppress current distortion due to grid voltage harmonics," *IEEE Trans. Power Electron.*, vol. 25, no. 12, pp. 3119–3127, Dec. 2010.
[44] M. Xue, Y. Zhang, Y. Kang, Y. Yi, S. Li, and F. Liu, "Full feedforward of grid voltage for discrete state feedback controlled grid-connected inverter with *LCL* filter," *IEEE Trans. Power Electron.*, vol. 27, no. 10, pp. 4234–4247, Oct. 2012.

Chenlei Bao was born in Zhejiang Province, China, in 1987. He received the B.S. degree from the School of Electrical Engineering and Automation from Harbin Institute of Technology, Harbin, China, in 2010, and the M.S. degree in electrical and electronic engineering from Huazhong University of Science and Technology, Wuhan, China, in 2013.

His current research interests include digital control technique and renewable energy generation system.

Xinbo Ruan (M'97–SM'02) was born in Hubei Province, China, in 1970. He received the B.S. and Ph.D. degrees in electrical engineering from Nanjing University of Aeronautics and Astronautics (NUAA), Nanjing, China, in 1991 and 1996, respectively.

In 1996, he joined the Faculty of Electrical Engineering Teaching and Research Division, NUAA, where he became a Professor in the College of Automation Engineering in 2002 and has been engaged in teaching and research in the field of power electronics. From August to October 2007, he was a Research Fellow in the Department of Electronic and Information Engineering, Hong Kong Polytechnic University, Hong Kong, China. Since March 2008, he has been also with the College of Electrical and Electronic Engineering, Huazhong University of Science and Technology, China. He is a Guest Professor with Beijing Jiaotong University, Beijing, China, Hefei University of Technology, Hefei, China, and Wuhan University, Wuhan, China. He is the author or coauthor of four books and more than 100 technical papers published in journals and conferences. His main research interests include soft-switching dc–dc converters, soft-switching inverters, power factor correction converters, modeling the converters, power electronics system integration, and renewable energy generation system.

Dr. Ruan was the recipient of the Delta Scholarship by the Delta Environment and Education Fund in 2003 and the recipient of the Special Appointed Professor of the Chang Jiang Scholars Program by the Ministry of Education, China, in 2007. Since 2005, he has been serving as a Vice President of the China Power Supply Society, and since 2008, he has been a member of the Technical Committee on Renewable Energy Systems within the IEEE Industrial Electronics Society. He has been an Associate Editor for the IEEE TRANSACTIONS ON INDUSTRIAL ELECTRONICS and the IEEE JOURNAL OF EMERGING AND SELECTED TOPICS ON POWER ELECTRONICS since 2011 and 2013, respectively. He is a Senior Member of the IEEE Power Electronics Society and the IEEE Industrial Electronics Society.

Xuehua Wang (M'12) was born in Hubei Province, China, in 1978. He received the B.S. degree in electrical engineering from Nanjing University of Technology, Nanjing, China, in 2001, and the M.S. and Ph.D. degrees in electrical engineering from Nanjing University of Aeronautics and Astronautics, Nanjing, China, in 2004 and 2008, respectively.

He is currently a Lecturer in the College of Electrical and Electronic Engineering, Huazhong University of Science and Technology, Wuhan, China. His main research interests include multilevel inverter and renewable energy generation system.

Weiwei Li (S'12) was born in Henan Province, China, in 1987. He received the B.S. degree in electrical and electronic engineering from Huazhong University of Science and Technology, Wuhan, China, in 2009, where he is currently working toward the Ph.D. degree.

His current research interests include digital control technique and renewable energy generation system.

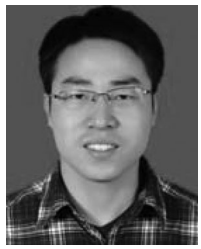

Donghua Pan (S'12) was born in Hubei Province, China, in 1987. He received the B.S. degree in electrical and electronic engineering from Huazhong University of Science and Technology, Wuhan, China, in 2010, where he is currently working toward the Ph.D. degree.

His current research interests include magnetic integration technique and renewable energy generation system.

Kailei Weng was born in Zhejiang Province, China, in 1987. He received the B.S. degree from the School of Electrical Engineering and Automation from Harbin Institute of Technology, Harbin, China, in 2011 and he is currently working toward the M.S. degree in electrical and electronic engineering in Huazhong University of Science and Technology, Wuhan, China.

His current research interests include digital control technique and renewable energy generation system.